

# A Computational Framework and an Algorithm for the Measurement of Visual Motion

P. ANANDAN

*Computer Science Department, Yale University, New Haven, CT 06520*

## Abstract

The robust measurement of visual motion from digitized image sequences has been an important but difficult problem in computer vision. This paper describes a hierarchical computational framework for the determination of dense displacement fields from a pair of images, and an algorithm consistent with that framework. Our framework is based on a scale-based separation of the image intensity information and the process of measuring motion. The large-scale intensity information is first used to obtain rough estimates of image motion, which are then refined by using intensity information at smaller scales. The estimates are in the form of displacement (or velocity) vectors for pixels and are accompanied by a direction-dependent confidence measure. A smoothness constraint is employed to propagate measurements with high confidence to neighboring areas where the confidences are low. At all levels, the computations are pixel-parallel, uniform across the image, and based on information from a small neighborhood of a pixel. Results of applying our algorithm to pairs of real images are included. In addition to our own matching algorithm, we also show that two different hierarchical gradient-based algorithms are consistent with our framework.

## 1 Introduction

### 1.1 Background

Motion is an important and fundamental source of visual information. It is well known that the pattern of image motion contains information useful for the determination of the three-dimensional structure of the environment and the relative motion between the camera and the objects in the scene. However, the accurate measurement of image motion from a sequence of real images has proved to be difficult.

While there seems to be widespread agreement that the measurement of motion should be based on primitive image events (such as intensity fluctuations, points, lines, etc.) and that it should be an early visual process, there seems to be less

agreement on its exact definition. In computer vision, the primary emphasis has been on the determination of instantaneous image velocities [17, 21,27,34] and the displacements of points between successive frames [8,22], although a few techniques have attempted to track lines and curves [26,43]. Recent developments in psychophysics, however, have focused on "spatiotemporal energy models" [1,25,40,41] which equate the measurement of motion with the measurement of spatiotemporal energy.

Although many of these techniques are based on solid theoretical foundations, they have generally not been successful in practice. The primary reason for the difficulty seems to be due to a lack of proper recognition of the fact that in discrete video sequences, the interframe image displacements are often considerably larger than one pixel. Also, if the scene contains multiple independently moving objects, the image motion may not be globally coherent, and there will be discontinuities in the image velocity (or displacement) field.

In this paper, we describe a hierarchical framework for the computation of dense displacement fields from a pair of images. We also describe a matching algorithm consistent with our framework and demonstrate its performance when applied to real images. A major contribution of our work is the synthesis of an orientation-selective confidence measure and a well-defined smoothness constraint within the hierarchical approach, thereby leading to a robust algorithm for measuring large interframe displacements. In addition, we have also adapted the “overlapped-pyramid” projection strategy [12] to improve our results, especially around locations of discontinuities in image motion.

An important reason for developing a computational framework is the unification of a variety of different techniques so that we may be able to identify the elements that are common to these techniques and recognize their differences. Historically, the gradient-based and the matching techniques have been seen as completely unrelated (or even somewhat opposed) to each other. We will show that the computational framework described here is sufficiently general that hierarchical versions of gradient-based algorithms are also consistent with it. In particular, the recent techniques of Enkelmann [17] and Glazer [21], which are, respectively, the hierarchical versions of the second-order technique of Nagel [35] and the first-order technique of Horn and Schunck [27] can be shown to contain all the components of our framework, although some of them in an implicit form.

## 1.2 Framework Overview

The key idea underlying our framework is the separation of computations according to scale. This idea is based on the following observation: usually, the large scale (or low spatial-frequency) intensity variations provide imprecise measurements over a large range of magnitudes of motion, while the small-scale (or high spatial-frequency) variations can provide more accurate measurements over a smaller range. This leads to three components of our framework: *spatial-frequency decomposition*, which is the method of separating

the intensity variations according to scale, a local, parallel *match criterion* within each scale, and a *control strategy*, which is a method for controlling the measurement processes at the different scales and combining their results.

Although the scale-based separation of computation provides a useful principle for processing scenes containing large displacements, there will always be situations when an image area lacks sufficient local information for displacement computation at a particular scale. Also, since the image displacement is a vector quantity, its reliability can vary according to direction. Therefore, another essential component of our framework is a direction-dependent *confidence measure*. The presence of unreliable displacements also means that in order to obtain a dense displacement field, it may be necessary to propagate the reliable displacements to their less reliable neighbors. This leads to the last essential component of our framework: a *smoothness constraint*, which specifies the criterion for the propagation of reliable displacements.

A visual illustration of this framework is provided in figure 1. The five major components mentioned in the above description are discussed in detail in section 2.

Readers familiar with the literature on motion and stereopsis will have already noticed the similarity of our framework to other past approaches for the measurement of motion, especially [14,22,29], and to the Marr-Poggio stereopsis algorithm [23,30]. In many ways, our work was inspired by these approaches; however, as it will become evident during the course of this paper, our technique differs from each of these past approaches in significant ways. For a detailed examination of the various approaches in the context of our framework, see [6].

## 1.3 Paper Organization

The detailed description of our framework for computing dense displacement fields from a pair of images is contained in section 2. First, the goals of the displacement computation are stated. This statement consists of specifying the nature of the input, the requirements on the output, and the

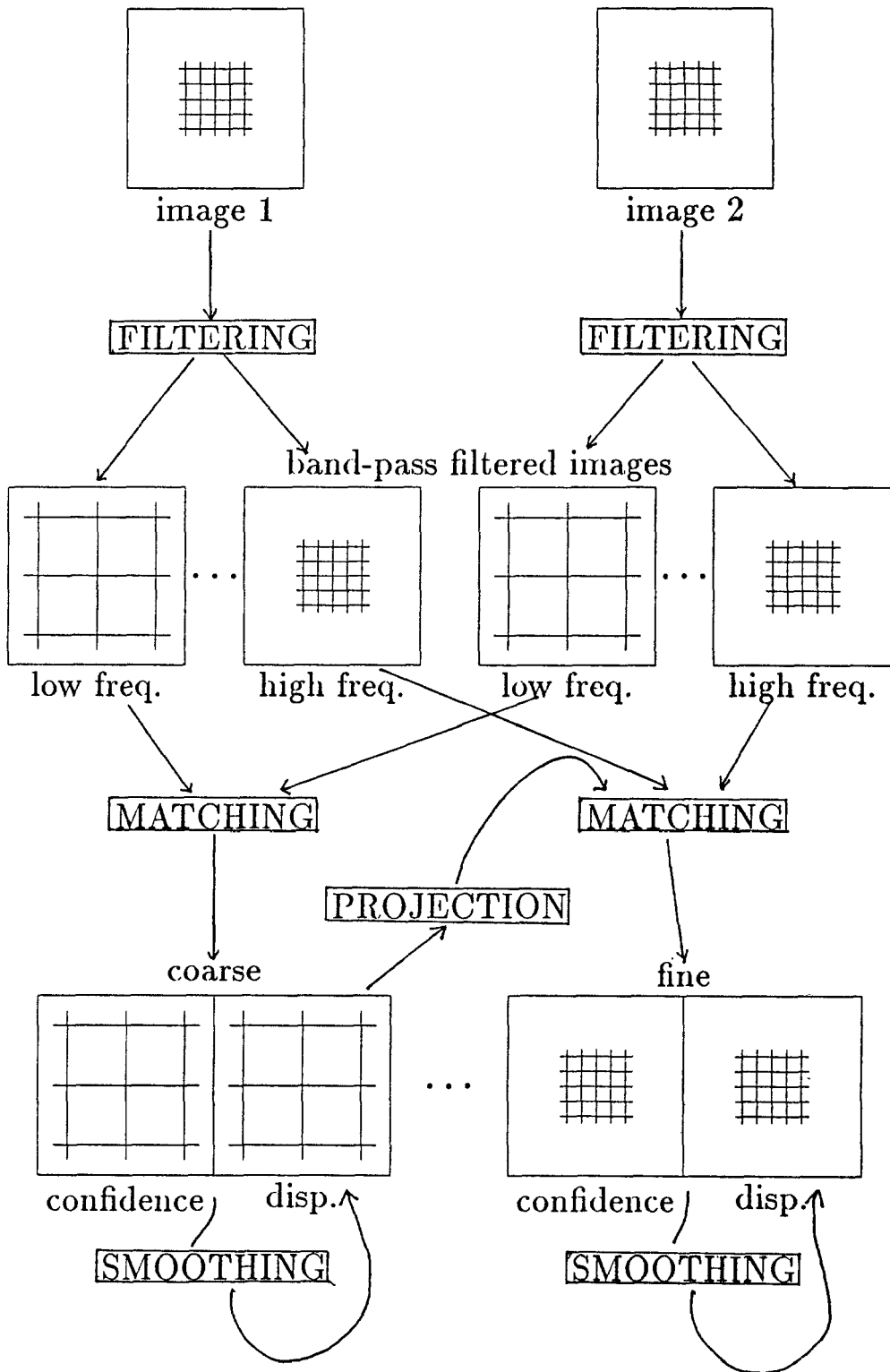


Fig. 1. The hierarchical computational framework.

computational constraints for this process. This is followed by the detailed descriptions of the five components of the framework.

Section 3 describes the specific choices made for the matching algorithm. Of these, the primary areas of our original contribution are the formulation of the confidence measure, the exact method of using the coarse-to-fine strategy, and the formulation of the smoothness constraint. Hence, the description will emphasize these aspects of our algorithm. Section 4 describes a set of experimental results obtained by applying this algorithm to two pairs of real images. While the success of the algorithm is immediately obvious upon visual inspection of these results, our discussion of these results focuses on the failures of this algorithm, so as to indicate the limitations that are inherent in our framework, and to some extent in any low-level approach to the measurement of motion.

Section 5 briefly outlines two hierarchical gradient-based approaches due to Glazer and Enkelmann respectively, and explains how these algorithms are consistent with our framework. In addition, section 5 also describes the mathematical relationship between the gradient-based techniques and the matching techniques. In section 6, we briefly discuss the issues involved in processing discontinuities in image motion, while section 7 contains a summary of the main ideas covered in the paper.

## 2 The Computational Framework

### 2.1 *The Computational Goals*

The goals of the process of computing image displacements are determined by three major factors: the nature of the image input, the requirements on the output, and constraints on computational efficiency. The input is a pair of digitized frames belonging to a discrete image sequence. The image displacements may be due to a general 3D motion of the camera or the independent motion of objects in the scene. The output should be a dense field of displacement vectors with associated confidence measures. All the computations must be pixel-parallel and use

local image information. We elaborate these points below.

*2.1.1 The Input.* In typical video sequences, the interframe displacements are usually considerably larger than a pixel. If independently moving objects are present, a single set of 3D motion parameters will not be consistent with the entire image. It may be possible to assume, however, that the objects in the environment are composed of continuous and opaque surfaces and that they undergo rigid or nearly rigid motions. These assumptions mean that (i) within the image area covered by a single surface, the displacement field varies smoothly, and (ii) the image motion can be described as “locally translational”, i.e., within a small area of the image, the displacement field can be approximated by a translational flow field. Thus, image sequences containing rotational motion can be processed, as long as the magnitude of rotation between frames is not large. Finally, we may also be able to assume that discontinuities in image motion occur at the boundaries of surfaces and objects.

It should be noted that the assumptions of opaqueness and near-rigid motions are essential for the successful performance of any algorithm based on our current computational framework. Although there are many situations (especially in indoor scenes) where such assumptions hold, it is clear there are cases (e.g., transparent surfaces, scenes with fences or trees) when they will be violated. In such cases, however, a purely “bottom-up” technique for measuring visual motion may be simply inappropriate; rather, a technique that simultaneously performs measurement and grouping may be necessary.

*2.1.2 The Output.* The requirement that the output should be a dense displacement field with an associated confidence measure is derived from the conclusions of the various studies concerning the problem of extracting structure from motion [2,3,18,42]. These studies indicate that a large number of image displacements are necessary for the accurate determination of the structure of the environment. If the scene contains independently moving objects, there may be no a priori knowledge of the image locations of such objects.

Therefore, the density of the displacement vector field should be uniformly high across the image, with a confidence measure indicating the reliability of each vector.

*2.1.3 Computational Considerations.* The considerations of computational efficiency and ease of implementation suggest that the following three properties are desirable for all computations: *parallelism*, *uniformity*, and *locality*.

Parallelism simply means that it should be possible to perform all computations simultaneously at all locations on the image plane. This is required in order to reduce the computational cost. Uniformity implies that the process should be similar at all locations. This is required because of the lack of a priori knowledge about image motion. In particular, it should be possible to describe any differences between the computations at different locations in terms of a few simple parameters. Locality means that the computations at any point on the image should be based on information local to that point. This is important in order to reduce the communication cost between processors, as well as to deal with the fact that the displacement field may not be globally coherent.

## 2.2 Spatial-frequency Decomposition

As noted briefly at the beginning of this paper, the key idea underlying the proposed computational strategy is the separation of computation on the basis of scale. Intuitively, it is clear that while small-scale intensity structures can be used to measure displacements over a short range, they may have many duplicate matches over a large range. This leads to ambiguities in the computation of the displacements. Therefore, in order to process large displacements, large-scale intensity information must be used. However, a single displacement computed on the basis of a large-scale intensity structure will be some form of the average of the displacements over the area covered by that structure and hence, its accuracy will be low. Such a “smoothed” displacement field will also vary slowly over the image plane and thus can

be sampled at a lower rate without loss of information.

These observations lead to the following principle: *large-scale image structures can be used to measure displacements over a large range with low accuracy and at a low sampling density, while small-scale image structures can be used to measure displacements over a short range with higher accuracy and at a higher sampling density.* An obvious way to enforce this principle is to decompose the image into its spatial-frequency components. Such a decomposition and the subsequent processing can be achieved by using a set of *spatial-frequency channels*.

Since the lower-frequency information can be sampled at a lower rate without any significant loss of information, the spatial-frequency decomposition process is usually accompanied by a corresponding reduction of resolution [11,47]. Such an approach leads to a pyramid representation of the spatial-frequency channels and fits naturally into a pyramid [28,37] or a processing-cone [24] architecture. However, since the final choice of a representation scheme depends on the type of hardware used, a pyramid representation is not an essential part of the framework.

## 2.3 The Match Criterion

As noted earlier, the *match criterion* is a method for determining the displacements within each channel. Since the displacement measured is small with respect to the scale of the intensity variations within a channel, a gradient-based approach can be used (see [17,21]). Alternatively, a correlation-matching approach [6,14,22] or a symbolic matching approach based on primitive tokens [23,30] can also be used. The separation of matching according to scale implies that the match criterion should have a *scaling* property—i.e., the measurement processes within different channels should be scaled versions of each other. Note that such a scaling property is directly provided in a pyramid representation.

## 2.4 The Control Strategy

The *control strategy* determines how the measurement processes at different scales are controlled

and how their results are combined. In our framework, the control strategy is based on a *spectral continuity* principle [23,32], which can be described as follows:<sup>1</sup> For images of opaque surfaces, it can be assumed that the displacement estimates at corresponding image locations in the different channels must be similar because they are due to relative motion between the camera and the same environmental area. This means that at any image location, a displacement computed from a high-frequency channel must be consistent with the estimates from the low-frequency channel at the corresponding image location.

A simple way of enforcing the principle of spectral continuity is with a coarse-to-fine control strategy. In this strategy, the processing proceeds from the low- to the high-frequency channels. The displacement estimate for a pixel in a low-frequency channel determines the center of the search area for the corresponding pixels in the next-higher-frequency channel. The scale invariance property of the measurement process suggests that the radius of the search areas between two adjacent channels should be proportional to the scale factor in order to ensure scale invariance of the computations. Once again, note that such scaling is automatically achieved in the pyramid representation.

### 2.5 *The Confidence Measure*

In general, there will be many areas of the image with insufficient information at a particular scale for the local determination of displacements. Therefore, a confidence measure should be computed along with each match at each scale to indicate whether or not to accept that match for further processing and also the degree to which the match can be trusted.

Since the image displacement is a vector quantity, it is possible that different directional components of the displacements may be locally computable with different degrees of reliability. For

instance, it is intuitively clear that in a homogeneous area of the image no component of the displacement can be reliably estimated. At a point along a line (or an edge), the component perpendicular to the line can be reliably computed, while the component parallel to the line may be ambiguous. Finally, at a point of high curvature along an image contour it may be possible to completely and reliably determine the displacement vector on the basis of local information. These observations suggest that the confidence measure should be directionally selective—i.e., that it should associate different confidences with the different directional components of the displacement vector. In addition, while an area may be homogeneous at one scale, it may have information useful for reliable matching at a different scale. Hence, the confidence measures should be separately computed within each spatial-frequency channel.

### 2.6 *Smoothness Constraint*

The computation of a dense displacement field will necessitate “filling in” areas with unreliable displacements. Such a filling-in process can be based on the assumption that the displacement field varies smoothly over the image area covered by a single surface. Thus, reliable displacements may be used to determine the values of less reliable neighbors.

The most common use of the smoothness assumption can be found in gradient-based techniques for determining image velocities. In these techniques, a smoothness constraint is formulated as a variational problem involving the minimization of an error associated with a velocity field. In our framework, we use a similar smoothness constraint *within every spatial-frequency channel*. After the displacements and the associated confidences are computed within each channel, the displacement field should be smoothed before it is projected to the next higher-frequency channel. During the smoothing process, the confidence measures should be used to retain the reliable displacements while allowing the less reliable estimates to change.

The smoothness assumption is violated at locations of discontinuities in the image motion.

<sup>1</sup>Note that this principle is usually violated wherever there is a discontinuity in image motion—i.e., in particular at surface and object boundaries. This issue is discussed in greater detail in section 6.

Such discontinuities arise at surface boundaries of a single object, or at object boundaries due to the independent movement of two different objects. Any scheme that uses the smoothness assumption should also include mechanisms for detecting such violations and processing them in an appropriate manner. We consider some approaches for the detection of discontinuities in section 6 of this paper. It should be noted that in general this remains a major unsolved problem.

### 3 The Hierarchical Matching Algorithm

In this section, we describe a matching algorithm that is consistent with our computational framework. There are five major components to the algorithm, corresponding to the five framework components described above. Of these, we will provide only brief outlines of the spatial-frequency decomposition, the match criterion, and the control strategy, since they are similar to well-known techniques in computer vision. The bulk of this section will focus on the confidence measure and the smoothness constraint, since their exact forms are rather new and, therefore, require more detailed discussion. For a detailed description of the entire algorithm the reader is referred to [6].

Any algorithm consistent with a computational framework will also be influenced by the architecture of the machine for which that algorithm is designed. As mentioned earlier, since pyramid representations and computations are naturally suited for our framework, our primary choice is a pyramid architecture [24,37]. However, it should be noted that we have also developed versions of the algorithm suitable for implementation on a simple mesh-connected computer [6,45].

For descriptive purposes, we have adopted the convention that the levels of the pyramid are numbered  $l = 0, 1, \dots$ , where, at any level  $l$ , the size of the processor array is  $2^l \times 2^l$ ; level 0 is called the "top" of the pyramid, while level  $L$  containing the input image is considered its "bottom."

#### 3.1 Spatial-Frequency Decomposition

A suitable method for spatial-frequency decomposition is provided by the Laplacian pyramid

transform proposed by Burt [11].<sup>2</sup> This algorithm consists of two stages: the first stage involves the construction of a Gaussian low-pass-filter pyramid from the input image, while the second stage involves computing the difference between the images at adjacent levels of the low-pass pyramid to obtain the set of band-pass-filtered images.

The finest level  $L$  of the Gaussian pyramid contains the input image. The image at any level  $l = L - 1, \dots, 0$  is formed by applying a  $5 \times 5$  Gaussian convolution operation to the image at level  $l + 1$  and subsampling the filtered image. The Laplacian pyramid image at level  $l$  is created by taking the pixel-wise difference between the Gaussian pyramid image at level  $l$  and the expanded version of the Gaussian pyramid image at level  $l - 1$ . For our algorithm, one such Laplacian pyramid is constructed from each input image.

#### 3.2 Match Criterion

The match criterion chosen was the minimization of a type of correlation measure. Correlation-based matching is a traditional, well-known approach in computer vision and image analysis. Apart from the fact that such a measure captures the intuitive notion of the similarity (or difference) between two intensity structures, it is simple to compute and is suitable for parallel and uniform computations. There are several types of correlation measures—e.g., direct correlation, mean-normalized correlation, variance-normalized correlation, and sum of squared differences (SSD). The definitions and the descriptions of these different measures can be found in [36]. An empirical study by Burt, Yen, and Xu [13] comparing these different correlation measures indicates that, when used on band-pass filtered images, the computationally simpler measures such as the direct correlation measure and SSD perform nearly as well as the more complex measures. The SSD measure is always positive, a fact that proved to be particularly useful when we considered the normalization of the confidence

<sup>2</sup>See [21] for a discussion of Burt's algorithm and other related algorithms for spatial frequency decomposition.

measure (described in section 3.4). Hence, our matching algorithm is based on the minimization of the SSD measure.

The exact details of the matching process are as follows: Within each processing level, each pixel in the first image is assigned a set of candidate matches according to the control strategy described in section 3.3. The SSD measure between each source and candidate pixel pair is determined by computing the Gaussian weighted sum of the squared differences between the values (from the Laplacian pyramid) of corresponding pixels in  $5 \times 5$  windows centered around the source and the candidate pixels. The best match for each source pixel is selected as the candidate with the minimum SSD.

Although correlation matching can fail dramatically when used in arbitrary situations, it appears to perform reasonably well when used within the spatial-frequency channels, particularly if the candidate matches are selected according to a hierarchical control strategy such as ours. Also, an important parameter is the window size. In a simple single-level correlation algorithm, the window size should increase with the width of the search area; otherwise, the likelihood of duplicate matches will increase. However, the use of band-pass filtering, pyramid representation, and the coarse-to-fine control strategy together allow us to use a single fixed-window size (in terms of number of pixels) for all points in the images at all levels of the Laplacian pyramid. Our choice of a  $5 \times 5$  window was based on a combination of theoretical and empirical reasons, which are described in detail in [6].

### 3.3 Control Strategy

The control strategy used in our algorithm is a coarse-to-fine sequential processing of the images in the Laplacian pyramid. In particular, we used an *overlapped pyramid* projection scheme, which is outlined below; a more detailed description can be found in [6].

If the input images are at level  $L$  of the pyramid and the maximum displacement of any pixel along either coordinate direction is less than  $\delta$ , the processing begins at level  $L - \log(\delta)$  and pro-

ceeds via sequential projection to image level  $L$ . At the coarsest level, no displacement exceeds a pixel. Hence, the search area is the  $3 \times 3$  pixel area centered around the corresponding pixel location in the second image. At all other levels, an initial set of displacements for a pixel are obtained by projecting the displacements from the adjacent coarser level. The search area is the  $3 \times 3$  area surrounding this projection.

The traditional approach (e.g., see [22]) used for the projection of displacements is based on the quad-tree type of connectivity between adjacent levels of the pyramid. The displacement at a pixel at level  $l - 1$  is projected to the four pixels below at level  $l$ . However, in this scheme, if the displacement computed for a coarse-level pixel is incorrect, the search areas of none of its descendants at any of the subsequent levels will contain its correct match. Hence, a single match error made at a coarse level causes a large block of pixels at the image resolution to have incorrect displacements.

To overcome some of the problems due to the quad-tree connectivity scheme, we have used an alternate scheme for projection of displacements, called the overlapped pyramid projection scheme. This scheme was used by Burt, Hong, and Rosenfeld [12] in connection with the problem of image segmentation. The displacement of a pixel at a coarse level  $l$  is transmitted to all the pixels in a  $4 \times 4$  area at the next finer level  $l + 1$ . Thus, each pixel at level  $l + 1$  obtains information from four pixels at level  $l$ , and can be regarded as having four potential parents—the parent of which it is a direct descendent and the three other parents whose projections are adjacent to it (see figure 2). The displacement of each of the four parents is considered a possible initial estimate for the search at level  $l$ ; often, however, two or more of these estimates will be identical. The search area consists of the union of the  $3 \times 3$  areas centered around each distinct coarse-level estimate, and the SSD measure is minimized over all the pixels in this expanded search area.

The advantage of using the overlapped pyramid projection algorithm is the following. Although a particular coarse-level pixel may be assigned an incorrect displacement, if the displacements of any of its neighbors are correct, the



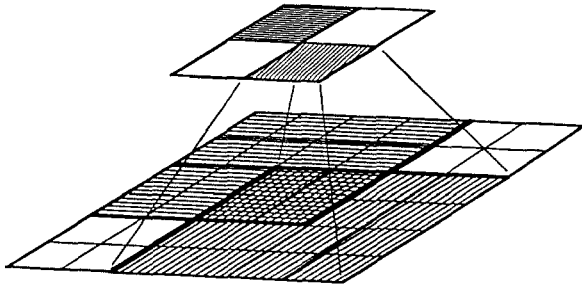


Fig. 2. The overlapped pyramid projection scheme.

search area for its descendents at the finer level will still contain their correct matches. A demonstration of the improvement in the results achieved by the use of this scheme can be found in [5].

In spite of the use of the overlapped pyramid projection scheme, there are still situations when the coarse-to-fine control strategy will lead to possibly avoidable mistakes at the finer levels. This issue is discussed further in section 6.

### 3.4 Confidence Measure

The confidence measure used in our algorithm is based on the variation of the SSD values over the set of candidate matches. Intuitively, it is clear that if the values of the SSD measures for different candidate matches are equal, then all those candidates are equally good matches. Thus, if the variation of the SSD measure along a particular line in the search area around the best-match pixel is small, then all the pixels along that line are equally good matches; i.e., the component of the displacement along the direction of that line cannot be uniquely determined. Also, if the SSD measure corresponding to the best match is large, then it is likely that even the best match is not a reliable match (implications of this are discussed later in this section).

Our approach for computing a confidence measure is based on the two intuitions mentioned above. In order to verify that the variation of the SSD measure reflects these properties, we conducted an empirical study involving a pair of syn-

thetic images. This section first describes the results of the empirical study; this is followed by a formal definition of the confidence measure and a discussion of its behavior in various typical situations encountered in real images.

**3.4.1 The Behavior of the SSD Surface.** The SSD surface is defined over the space of displacements, and its height is the SSD value corresponding to each displacement. For our empirical study, we created a pair of synthetic images by digitally “cutting and pasting” pieces from two real images photographed in the robotics laboratory at the University of Massachusetts. We selected a number of specific points corresponding to typical image structures such as corners, edges, homogeneous areas, and occluded areas, and studied the behavior of the SSD surface computed based on the finest-level images of the Laplacian pyramids created from the input images.

The details of our study are too long for this paper, and can be found in [6]. Figures 3, 4, 5, and 6 are examples of SSD surfaces. Figure 3 shows the SSD surface at an intensity corner; figure 4 shows the surface at an edge; figure 5 shows the surface at a point in an area of homogeneous intensity; and figure 6 shows the shape of the surface at an occluded corner point. The surfaces are

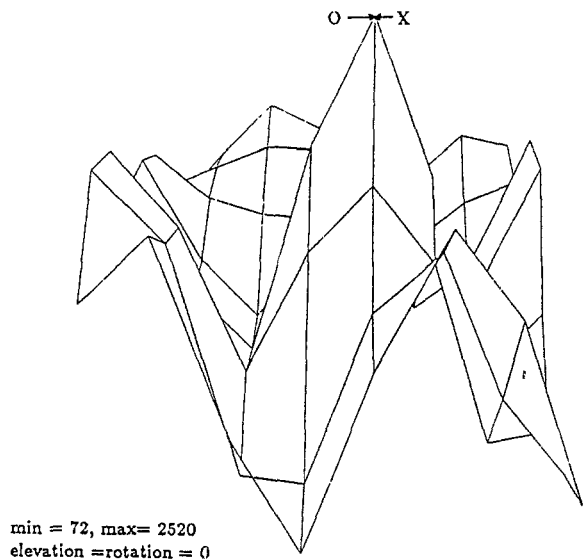


Fig. 3. The SSD surface at a corner point.

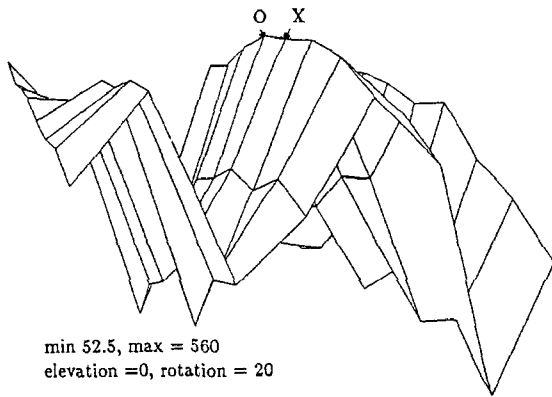


Fig. 4. The SSD surface at an edge point.

shown inverted in order to enhance visibility; the viewing position of the surface is noted in each figure; and the maximum and minimum elevations of the surface are indicated. In each figure, we have also marked the point of minimum SSD value with the symbol "O", and the point corresponding to the correct displacement with an "X."

From the figures shown it is evident that at the corner point the SSD surface shows a unique peak (in actuality, a minimum), and that the location of the minimum corresponds to the correct displacement. In the case of the edge-like point, a ridge-like structure is seen, and the location of the minimum along the ridge seems ambiguous; this

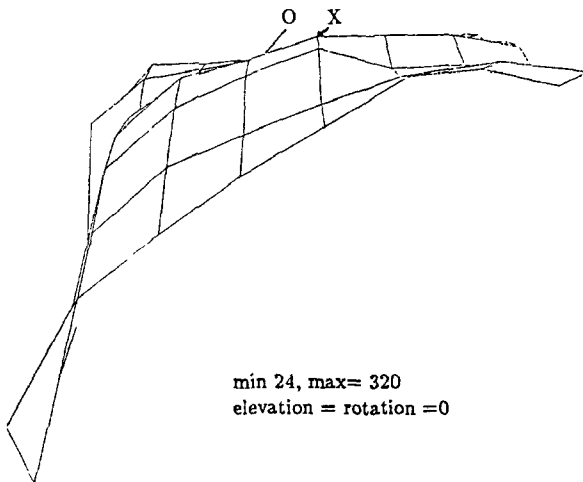


Fig. 5. The SSD surface at a point in a homogeneous area:

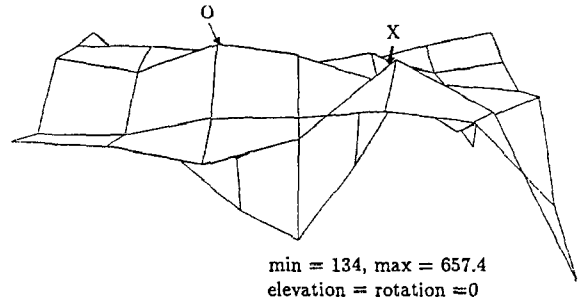


Fig. 6. The SSD surface at a corner point that is occluded in the second frame.

suggests that the component of the displacement vector in the direction parallel to the ridge is uncertain. At the homogeneous area the SSD measure shows very little variation, suggesting that the selection of a unique match is impossible. Finally, the shape of the SSD surface at the occluded corner point is erratic, indicating that the match may be entirely unreliable.

The types of shapes of the SSD surface illustrated in the accompanying figures, and described above, were observed over many images. In particular, the curvatures of the SSD surface along particular directions were usually large (or small) when the corresponding component of the displacement vector were correct (or incorrect). The formal definition of the confidence measure given below is based on these observations.

**3.4.2 Definition of the Confidence Measure.** The curvature of a surface at a point along any arbitrary direction can be determined if the two *principal curvatures* at that point and the directions of the associated *principal axes* are known [15]. The principal axes are defined as the directions along which the curvature of the surface is either a maximum or a minimum, and the principal curvatures are the curvatures of the surface along those directions. We denote the maximum principal axis by the unit vector  $\hat{e}_{max}$  and the associated curvature as  $C_{max}$ , and the minimum principal axis by the unit vector  $\hat{e}_{min}$  and the associated curvature as  $C_{min}$ .<sup>3</sup>

<sup>3</sup>We have followed the notational convention of using boldface lowercase letters for vectors, boldface lowercase letters with "hats" for unit vectors, boldface uppercase letters for matrixes, and nonboldface letters for scalars.

Our confidence measure consists of two magnitudes (called “confidences”)— $c_{\max}$  and  $c_{\min}$ , and two directions (or unit vectors)— $\hat{e}_{\max}$  and  $\hat{e}_{\min}$ . As mentioned above, the unit vectors denote the principal axes of the SSD surface, while

$$c_{\max} = \frac{C_{\max}}{k_1 + k_2 S_{\min} + k_3 C_{\max}}$$

and

$$c_{\min} = \frac{C_{\min}}{k_1 + k_2 S_{\min} + k_3 C_{\min}}$$

where  $k_1, k_2$ , and  $k_3$  are normalization parameters, and  $S_{\min}$  is the SSD value corresponding to the best match.

The exact form of the normalization function was derived from the following considerations. The confidence measure is made proportional to the corresponding principal curvature according to the intuition that the reliability of the displacement should be proportional to the curvature of the SSD surface. Since a large value for  $S_{\min}$  indicates an unreliable match due to occlusion, noise, or deformation of the image area, the confidence is inversely proportional to  $S_{\min}$ . The presence of the term containing the curvature in the denominator is useful to maintain the confidence value in the range  $(0, 1/k_3)$ . If it is desired not to restrict the range,  $k_3$  can be set to zero. The constant term  $k_1$  is used to maintain a finite value for the confidence measure when  $S_{\min}$  tends to zero.

Computation of the principal curvatures involves knowing the second partial derivatives of the SSD surface along the coordinate directions. Given that we have a discrete set of SSD values, we need to introduce a specific surface-fitting model and an appropriate window size for the fit. The minimum window size necessary to numerically determine the second derivatives is  $3 \times 3$ . Although a larger window may yield more reliable estimates, the attendant computational cost is higher. Hence we used a  $3 \times 3$  set of SSD values around the best match as our data, and determined the quadratic surface that fit that data by using a best-least-square method due to Beaudet [9]. This method involves computing weighted sums of the  $3 \times 3$  values to obtain the various first- and second-order derivatives of a surface. The principal curvatures can be ex-

pressed as nonlinear combinations of the second derivatives.

**3.4.3 Discussion.** Intuitively, the vectors  $\hat{e}_{\max}$  and  $\hat{e}_{\min}$  and the confidences  $c_{\max}$  and  $c_{\min}$  can be understood as follows: At a point along an edge in the image, the vector  $\hat{e}_{\max}$  will be approximately oriented in the direction normal to the edge, and  $\hat{e}_{\min}$  will be oriented parallel to the edge. At such a point,  $c_{\max}$  will be large and  $c_{\min}$  will be small. On the other hand; in an area of the image with small intensity variations, both the measures will be small, whereas at a point along a contour with high curvature, both will be high.

An important issue that was somewhat sidestepped in this section was the sensitivity to occlusion. Although we have so far assumed that a large value for  $S_{\min}$  indicates a “false match” (i.e., a match does not exist), in general  $S_{\min}$  can be large due to a variety of reasons. Some of these reasons are listed below:

1. The search area does not contain the true match, either because of an incorrect initial displacement or because of occlusion.
2. The template window contains a discontinuity in image flow. This arises at points near depth or motion discontinuities. In this case, since the window straddles the boundary, the intensity structure within the window varies between frames.
3. The magnitudes of rotation and/or the translation in depth are large or the image area undergoes nonrigid motion. In this case, the template window undergoes an area deformation, which violates the assumption of locally translational motion.
4. The SNR (signal-to-noise ratio) is low. In this case, the intensity values of corresponding areas in the two images differ due to the presence of noise.

In all the cases listed above,  $S_{\min}$  will be large only if the local “spectral energy” (i.e., the RMS value of the intensities in the template window) is large. A small value for the spectral energy suggests that the intensity varies very little—i.e., the point is in a homogeneous intensity area; hence, all the values on the SSD surface will be uniformly small.

Finally, at a homogeneous occluded area,  $S_{\min}$

will be small, even though the match estimate will usually be incorrect. As noted above, this arises due to the low spectral energy of the area. In these cases, the curvatures of the SSD surface may also be low, thereby making our confidence measures small. However, if the occluded homogeneous area straddles a textured area (where the spectral energy is high), then the curvatures of the SSD surface may be large, because the displacements on one side of the best match will have large SSD values, since they are a result of comparing a homogeneous area with a textured area. Therefore, although no match for the occluded point exists in the second image, the confidence measure may be large for some (incorrect) match in the homogeneous area of the second image. The estimated displacement is likely to equal the relative displacement between the textured area and the homogeneous area. Thus, there may be points in homogeneous areas that are occluded by textured areas, where our matching process may provide incorrect displacements with high values for the confidence measures. This type of problem seems not to have been considered seriously in the literature on the measurement of motion, perhaps because the idea of using explicit confidence measures is uncommon.<sup>4</sup>

During our empirical study of the SSD surfaces [6], we also observed that the shapes of the auto- and the cross-SSD surfaces are usually different for most occluded areas. Therefore, an additional clue for the presence of occlusion may be obtained by comparing the shape of these two surfaces. We expect to further develop these and other ideas for the detection of false matches during our own future research on the measurement of image motion.

### 3.5 Smoothness Constraint

The problem of finding a smooth displacement field that approximates the displacement estimates computed at a discrete set of points by the local match process can be formulated as a minimization problem. That is, a vector field  $\{\mathbf{u}\}$

is needed which minimizes a quadratic functional  $E(\{\mathbf{u}\}) = E_{\text{sm}}(\{\mathbf{u}\}) + E_{\text{ap}}(\{\mathbf{u}\})$  where the smoothness error  $E_{\text{sm}}$  measures the spatial variation of  $\{\mathbf{u}\}$  and the ‘‘approximation error’’  $E_{\text{ap}}$  measures how well  $\{\mathbf{u}\}$  approximates the set of displacements provided by the matching process.

Intuitively, a displacement field can be considered smooth in an area of the image if its variation over the area is small. An example of a measure of the spatial variation of a displacement field is

$$\begin{aligned} E_{\text{sm}}(\{\mathbf{u}\}) &= \iint \text{trace} \{(\nabla \mathbf{u}^T)^T (\nabla \mathbf{u}^T)\} dx dy \\ &= \iint (u_x^2 + u_y^2 + v_x^2 + v_y^2) dx dy \quad (1) \end{aligned}$$

where  $\{\mathbf{u}\}$  is the set of the displacement vectors  $\mathbf{u}(x,y) = (u(x,y), v(x,y))^T$ , and  $\nabla$  represents the gradient operator. The domain of integration is usually the whole image. For notational convenience, we have used  $\mathbf{u}$  to mean the vector  $\mathbf{u}(x,y)$ . The above formulation of a smoothness error is due to Horn and Schunck [27], who used this measure in a gradient-based approach for the computation of optical flow. Other examples of such measures will be discussed later in this section.

Let  $\{\mathbf{d}\}$  be the set of estimates provided by the match process; these are represented in the local orthogonal basis  $(\hat{\mathbf{e}}_{\text{max}}, \hat{\mathbf{e}}_{\text{min}})$ , which denote the principal axes of the SSD surface. For a given displacement field  $\{\mathbf{u}\}$ , the approximation error is a weighted sum of the deviations of the components of the displacement vectors  $\mathbf{u}(x,y)$  of the field along the basis directions from the corresponding components of the match estimates  $\mathbf{d}(x,y)$ . The weights are the confidences  $c_{\text{max}}$  and  $c_{\text{min}}$ . Mathematically,

$$\begin{aligned} E_{\text{ap}}(\{\mathbf{u}\}) &= \sum_{x,y} [c_{\text{max}}(\mathbf{u} \cdot \hat{\mathbf{e}}_{\text{max}} - \mathbf{d} \cdot \hat{\mathbf{e}}_{\text{max}})^2 \\ &\quad + c_{\text{min}}(\mathbf{u} \cdot \hat{\mathbf{e}}_{\text{min}} - \mathbf{d} \cdot \hat{\mathbf{e}}_{\text{min}})^2] \quad (2) \end{aligned}$$

Note that our formulation of  $E_{\text{sm}}$  implies that the space of admissible functions are a subclass of  $C_0$  functions. The following alternate form, which regards the admissible functions as a subclass of  $C_1$  functions, is also possible:

<sup>4</sup>There are, however, examples of confidence measures being used for disparity measurements—see [20] for an example.

$$E_{sm} = \iint (u_{xx}^2 + 2u_{xy} + u_{yy}^2 + v_{xx}^2 + 2v_{xy} + v_{yy}^2) dx dy \quad (3)$$

Although we have also implemented an algorithm based on this formulation (see [7]), most of our experiments have been based on the simpler formulation given above in equation (1). This is because results from early experiments with the two formulations did not show significant qualitative differences, while the solution to the second-order formulation given above requires more computational effort.

**3.5.1 Solving the Minimization Problem.** The two functionals  $E_{sm}$  and  $E_{ap}$  have been chosen in such a manner that under certain weak conditions there will always exist a unique solution for our minimization problem. In particular, it is easy to show that a unique minimum exists if there is at least one corner point in the image (both  $c_{max}$  and  $c_{min}$  are nonzero), and/or there are two points with different  $\hat{e}_{max}$  vectors. A proof can be found in [6].

The most common approaches for solving the variational problem formulated here are the finite-difference method, a type of gradient-descent approach, and the finite-element method. For instance, Horn and Schunck [27], Glazer [21], and Nagel [35] all have used the finite-difference method. Hildreth [26] has used the conjugate-gradient approach, while Terzopoulos [38] has used the finite-element method for his surface reconstruction problem. We have also chosen the finite-element method because it has a well-developed theory for the inclusion of known discontinuities in the field.

The basic idea behind the finite-element method is the tessellation of the image plane using a set of elements with predefined shapes, and representing the field using piecewise polynomials defined over these elements. The order of the polynomials is determined according to the order of the derivatives involved in the error functional. A key requirement is that the discrete solution should converge to the true minimum as the element sizes tend to zero.

Terzopoulos has developed finite-element method algorithms for both first- and second-

order smoothness constraints for the surface-interpolation problem. Since our variational problem can be regarded as a vector generalization of his scalar formulation, his solution methods can also be adapted. Since we have adapted Terzopoulos' approach for solving the variational problem, we do not discuss the mathematical details here. A clear description of such an analysis can be found in chapters 5 and 6 of [38]. Here, we simply describe the steps involved in our algorithmic implementation.

**3.5.2 Computation of Masks.** In order to solve the discrete minimization problem, linear equations in the values at the nodes of a square grid (which is in registration with the image array) are derived. These equations are used to update the values  $\mathbf{u} = (u, v)$  at a point in terms of its neighbors. In particular, solving the discrete problem can be shown to be the same as solving the following system of coupled equations:

$$(\mathbf{u} - \bar{\mathbf{u}}) + c_{max}(\mathbf{u} \cdot \hat{e}_{max} - \mathbf{d} \cdot \hat{e}_{max})\hat{e}_{max} + c_{min}(\mathbf{u} \cdot \hat{e}_{min} - \mathbf{d} \cdot \hat{e}_{min})\hat{e}_{min} = 0 \quad (4)$$

where for each point on the grid,  $\bar{\mathbf{u}}$  is a weighted average of the displacements of its neighbors. For the first-order smoothness constraint the weights are distributed as follows:

$$\frac{1}{4} \times \begin{matrix} 1 & & \\ 1 & 0 & 1 \\ & 1 & \end{matrix}$$

**3.5.3 Relaxation Algorithm.** There are a number of numerical methods for solving the system of coupled linear equations described above. One of the simplest methods is the Gauss-Seidel relaxation algorithm. This is an iterative process, where during each iteration the value of  $\mathbf{u}$  at each point in the image is solved in terms of the values of its neighbors.

The iterative update equation for the displacement field smoothing problem is,

$$\mathbf{u}^{n+1} = \bar{\mathbf{u}}^n + \frac{c_{max}}{c_{max} + 1} ((\mathbf{d} - \bar{\mathbf{u}}^n) \cdot \hat{e}_{max})\hat{e}_{max} + \frac{c_{min}}{c_{min} + 1} ((\mathbf{d} - \bar{\mathbf{u}}^n) \cdot \hat{e}_{min})\hat{e}_{min} \quad (5)$$

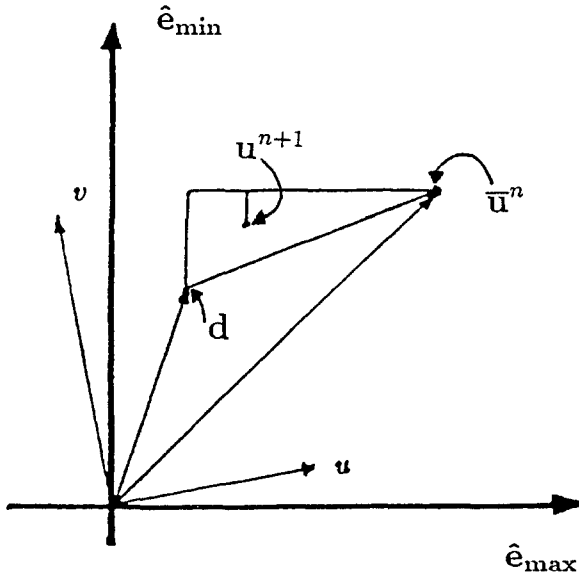


Fig. 7. A geometric interpretation of the relaxation process.

where the superscripts denote the number of the iteration.

The updating scheme described above has the following geometric interpretation:  $\mathbf{u}^{n+1}$  is a point in the  $(u, v)$  space which is a combination of  $\bar{\mathbf{u}}^n$  and  $\mathbf{d}$ . The manner in which this combination takes place is illustrated in figure 7, where the displacements have been represented in a cartesian coordinate system with its axes parallel to  $(\hat{e}_{\max}, \hat{e}_{\min})$ . Since  $c_{\max} \geq c_{\min}$ , the location of  $\mathbf{u}^{n+1}$  will always be on or above the line joining  $\mathbf{d}$  and  $\bar{\mathbf{u}}^n$ . In particular, it can be seen that  $\mathbf{u}^{n+1}$  will always be within the triangle shown in the figure, moving toward the line joining  $\mathbf{d}$  and  $\bar{\mathbf{u}}^n$  as  $c_{\min}$  gets closer to  $c_{\max}$ .

The two key parameters are  $c_{\max}/(1 + c_{\max})$  and  $c_{\min}/(1 + c_{\min})$ , which vary between 0 and 1, as  $c_{\max}$  and  $c_{\min}$  vary between 0 and  $\infty$ . When  $c/(1 + c)$  (where  $c = c_{\max}$  or  $c_{\min}$  appropriately), is close to zero, the updated value is close to the average of the neighbors, whereas when it is close to 1, the updated value is close to the initial local displacement estimate. The function  $c/(1 + c)$  rises rapidly and approaches its maximum value, 1, so that even a small value of  $c$  (e.g., 10) orients the updated value strongly ( $c/(1 + c) = 0.91$ ) toward the

initial local estimate. For our experiment, the choice of the normalization parameters for the confidence measures was based on this observation concerning the behavior of the updating algorithm.

Finally, note that during the projection of the displacements to the next-finer-level, the values will be rounded to the nearest integer value; hence, it is not necessary to wait until the complete convergence of the smoothing algorithm. The relaxation process can be stopped when the rounded-off values of the displacements do not change during an iteration. In practice, we found that 10 iterations were usually sufficient to achieve this condition.

## 4 Experimental Results

This section describes the results applying the ideas described in this paper to two pairs of real images. The two experiments are called the *dinosaur-image experiment* and the *hallway-scene experiment*.

The key parameters involved in the computation of our confidence measures are the normalization coefficients  $k_1$ ,  $k_2$ , and  $k_3$ . For our experiment, we chose  $k_1 = 150$ ,  $k_2 = 1$ , and  $k_3 = 0$ . As noted in section 3.4,  $k_1$  is an overall scaling factor,  $k_2$  controls the influence of  $S_{\min}$ , and  $k_3$  is useful to restrict the range of the confidence values. The choice of  $k_3 = 0$  simply means that the ranges of the confidences are unrestricted. The choice of  $k_2 = 1$  means that the influence of  $S_{\min}$  is of the same order as that of the curvatures. Our choice of  $k_1 = 150$  was based on the empirical observation that the mean values of  $C_{\max}$  was between 100 and 200. Therefore, barring the effects of  $S_{\min}$ , on the average  $c_{\max}$  will be approximately 1, and the factor  $c_{\max}/(1 + c_{\max})$  will be approximately  $1/2$ . This means that on the average, the local displacement estimate and the weighted average of the neighbors' estimates have equal effect during each iteration of the relaxation process.

### 4.1 The Dinosaur-Image Experiment

The input images used in this experiment are the two  $128 \times 128$  resolution images shown in figure 8.

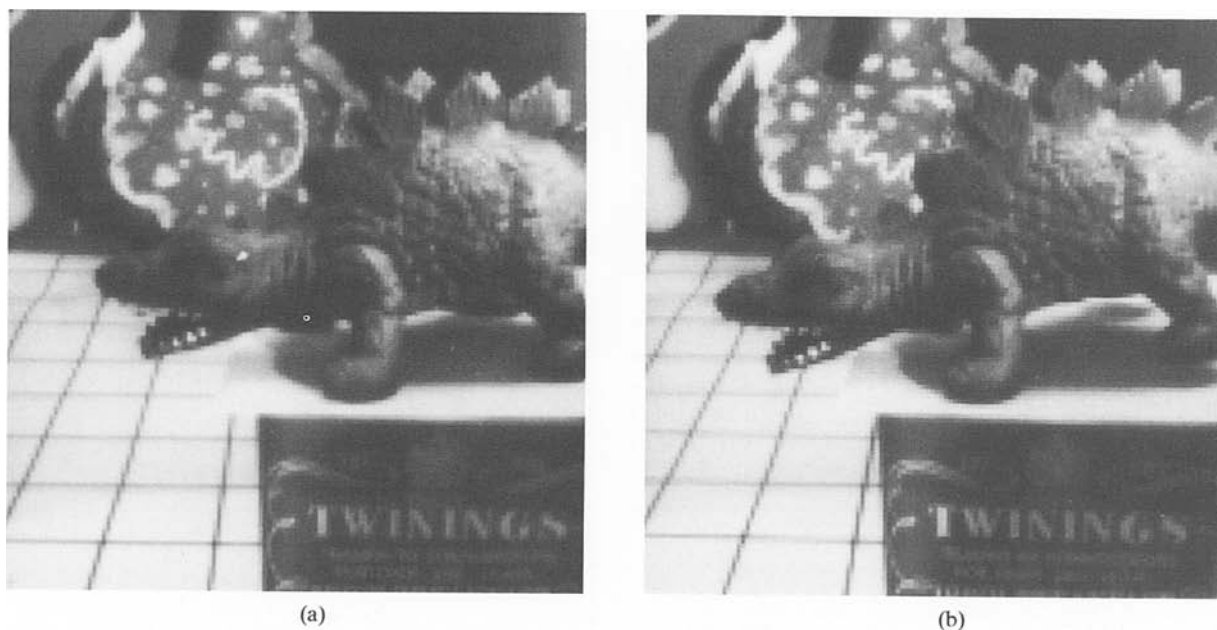


Fig. 8. The dinosaur-image experiment—input.

The scene consists of a toy dinosaur, a toy chicken in the background, and a tea box in the foreground, all of which rest on a table top which has a grid pattern on it. The toy chicken, which is somewhat hard to see in the images shown here, is behind the neck area of the toy dinosaur. The 3D motion between the two frames consists of a translation of the camera to the right along with a leftward rotation of  $1.5^\circ$  about the vertical axis (in order to bring the scene back into view), as well as an independent  $4.2^\circ$  anticlockwise rotation of the dinosaur about the optical axis. The magnitudes of the image displacements induced by these 3D motions are as follows: the toy chicken appears to have moved right by about 3 to 5 pixels; the tea can appears to have moved left by about 4 to 6 pixels; the grid pattern on the floor is almost stationary; and the points on the surface of the dinosaur appear to have moved by about 7 to 10 pixels. This scene is of interest for the obvious reason that it contains a distinct and prominent independently moving object besides containing a complex camera motion.

Figure 9 shows the displacement fields at the four levels of the pyramid computed by the

hierarchical matching process *without* smoothing, while figure 10 displays the displacement field at the same four levels produced by the hierarchical algorithm *with* smoothing. Figure 11 displays the displacement field at the finest resolution superimposed on the first frame. Figure 12 displays the confidence measure  $c_{\max}$  at the four levels with the direction vectors  $\hat{e}_{\max}$  superimposed, as well as the confidence measure  $c_{\min}$ .

Qualitatively, figure 11 shows that the algorithm performs remarkably well in this real image containing complex motion. Note that while the toy chicken and the tea box undergo the same 3D relative motion with respect to the camera, (i.e., a translation parallel to the image plane combined with a rotation about the vertical axis), the movement of their images appears to be in opposite directions. This is because, while the leftward rotation of the camera induces a rightward image flow in both the regions, the effect of the compensatory rightward translation is greater on the image of the tea box, since it is closer to the camera. Figure 11 shows that our algorithm has correctly determined the image displacements of

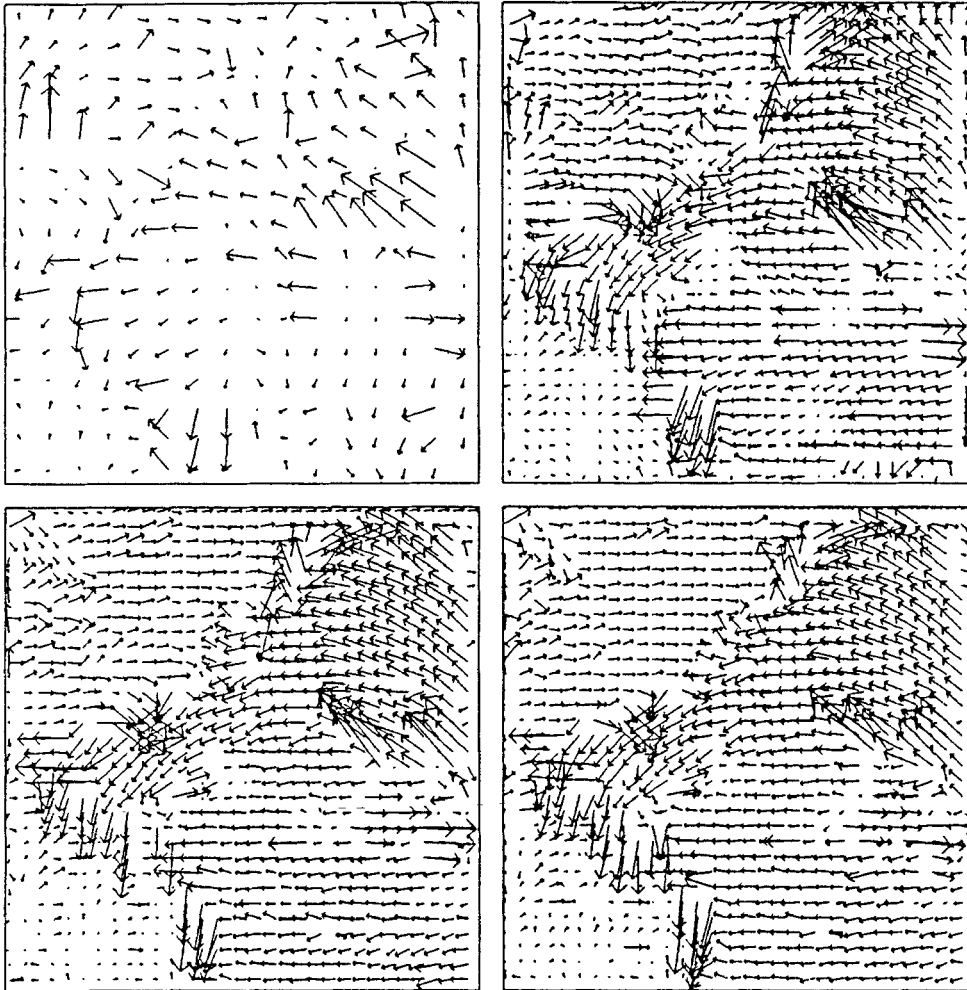


*Fig. 9.* The dinosaur-image experiment—unsmoothed results. The results of the dinosaur-image experiment without smoothing and with  $5 \times 5$  Gaussian template windows. The top left and right quadrants contain results from levels 4 and 5 respectively, while the bottom left and right quadrants contain the results from levels 6 and 7. In order to enhance visibility, only a  $32 \times 32$  sample of the displacements has been shown at levels 6 and 7.

these two objects. It is also clear that the independent movement of the dinosaur has been successfully computed. The expected behaviors of the confidence measures at corners, edges, and homogeneous areas are confirmed by the displays in figure 12.

The improvement obtained by the smoothing process is easily seen by comparing the results shown in figures 9 and 10. Note that at the two coarsest resolutions, the displacement field has been smoothed across surface and object bound-

daries, whereas at the finer levels there are sudden changes near such boundaries. This is due to the use of the overlapped pyramid projection strategy, as well as the fact that the input images contain significant contrast at high frequencies. Hence, the finer-level matching processes were able to correct some of the errors made at the coarser levels. In particular, note that the boundary between the chicken and the dinosaur has been maintained during the finer-level smoothing processes, primarily due to the proper de-



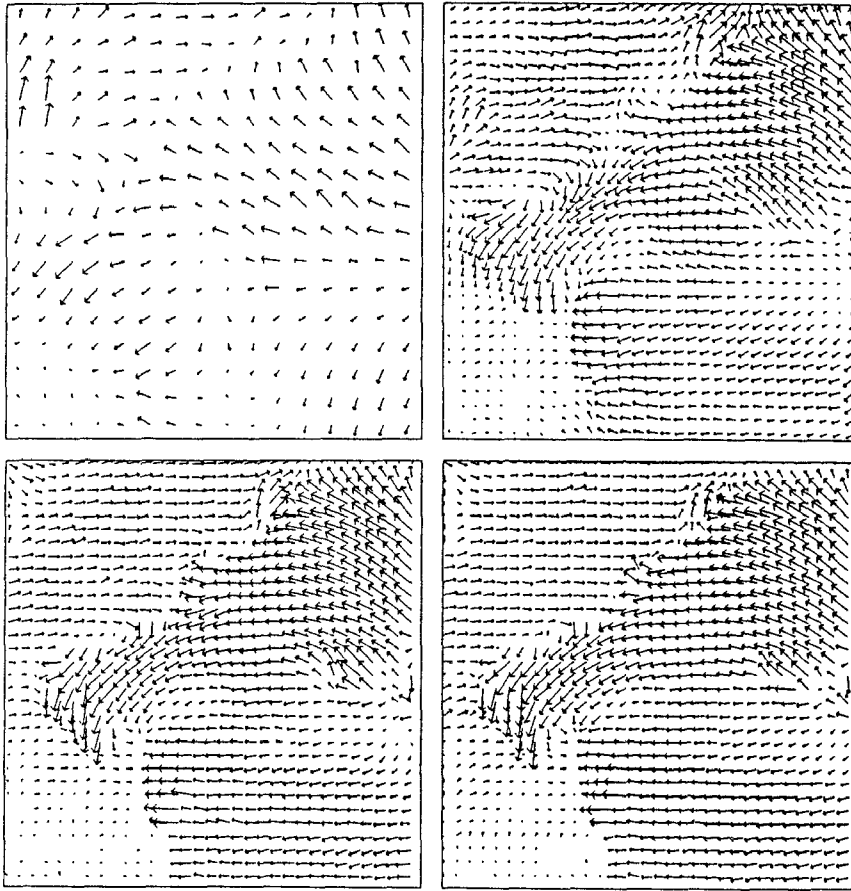


Fig. 10. The dinosaur-image experiment—smoothed results. The results of the dinosaur-image experiment with smoothing and with  $5 \times 5$  Gaussian template windows. Once again, the top left and right quadrants contain results from levels 4 and 5 respectively, while the bottom left and right quadrants contain the results from levels 6 and 7. Also, only a  $32 \times 32$  sample of the displacements has been shown at levels 6 and 7.

coupling via the confidence measures.

Although the area on top of the dinosaur is part of the background, the vectors in that area seem to be influenced by the motion of the dinosaur. Similarly, the area of the floor just left of the tea box has displacements that are obviously incorrect. This is because both these areas are somewhat homogeneous, and are adjacent to areas containing high-contrast information. In addition, parts of the floor have been occluded, or are near the occlusion boundary, and therefore do not have reliable local estimates. Hence, the more-reliable neighboring vectors have been

propagated by the smoothing process to these areas with unreliable local estimates. Such problems due to occlusion are pervasive in the field of motion analysis.

Note that near the displacements on one of the lines of the grid pattern near the top of the tea box (which is visible in both frames) are obviously incorrect. This error occurs because the vertical line on the floor is adjacent to the occlusion boundary, and the intensity structure of its neighborhood undergoes significant changes between the two frames. The problems here have been made more severe by the use of a coarse-to-fine control

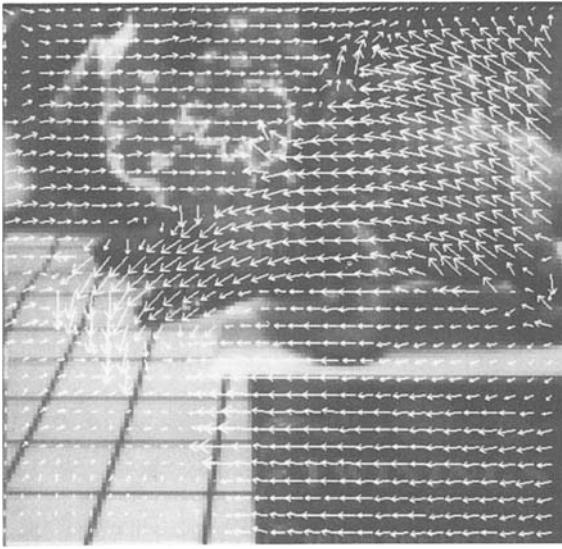
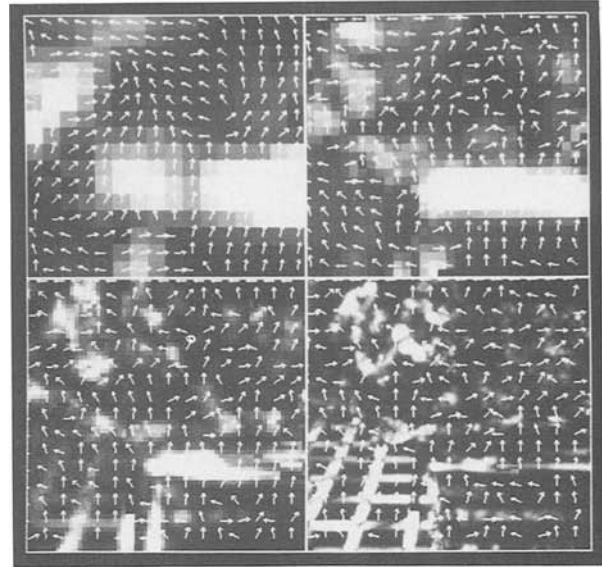


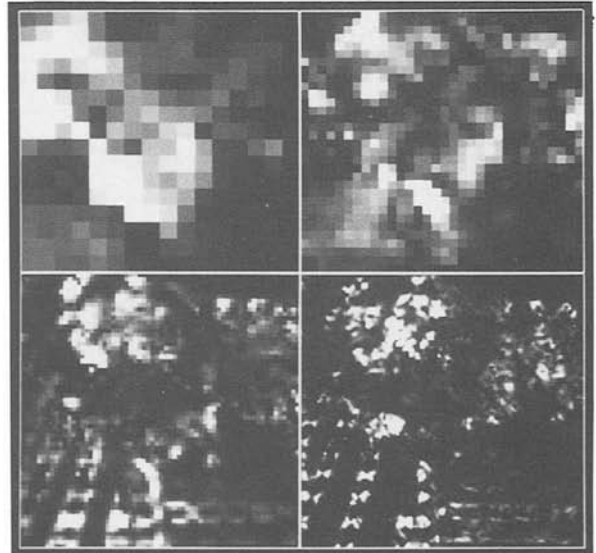
Fig. 11. The dinosaur-image experiment—finest-level results. The smoothed displacement-vector field at the finest level for the dinosaur-image experiment superimposed on the first input frame. In order to enhance visibility, only a  $32 \times 32$  sample of the displacements has been shown.

strategy, since at low frequencies the area affected by the occlusion increases; it appears that even the use of the overlapped pyramid projection strategy has not corrected these errors. However, as illustrated in figure 12, the confidences associated with the incorrect displacements on the line are small.

The area of the floor just below the nose of the dinosaur also has incorrect displacements. In this case, however, the problem is not due to the smoothness constraint. Instead, it arises because the grid pattern on the floor is periodic, and the difference in the displacement of the nose of the dinosaur and the floor is approximately equal to the period of the grid pattern. Hence, at the coarse levels of processing, the grid pattern near the nose of the dinosaur appears to have moved one period, whereas its actual image motion is much smaller (almost zero). This may be a harder problem to solve by a low-level two-frame matching technique, because all displacements that are multiples of the period of the grid pattern are equally valid. In order to resolve them, either higher-level texture-based grouping processes, or



(a)



(b)

Fig. 12. The dinosaur-image experiment—confidence measures. The confidence measures are computed in the dinosaur-image experiment with smoothing. The confidence measures are shown at the four finest levels. (a) Shows  $c_{\max}$  and samples of  $\hat{e}_{\max}$ . (b) Displays  $c_{\min}$ .



(a)



(b)

*Fig. 13.* The hallway-scene experiment—input images.

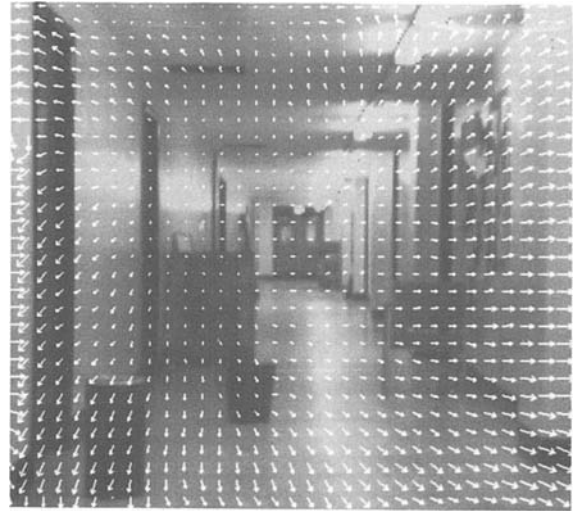


*Fig. 14.* The hallway-scene experiments—finest-level results. The finest-level displacements for the hallway-scene experiment are superimposed on the first input frame. In order to enhance visibility, only a  $32 \times 32$  sample of the displacements has been shown.

constraints involving the temporal coherence of the movement may be necessary. For a discussion of the mechanisms for incorporating the temporal coherence assumption, refer to [6].

#### *4.2 The Hallway-Scene Experiment*

The input images for this experiment are shown in figure 13. These  $256 \times 256$  pixel resolution images were produced at the UMass Computer Vision Laboratory. Once again all image motion is due to a camera undergoing translational motion. The reason for choosing this image pair is the presence of the many long linear structures in the image. Since the confidence measure separates such areas from corners and homogeneous areas, it is interesting to study its behavior in this experiment.

For the sake of brevity, we only show the results of the algorithm with smoothing at the finest level. Figure 14 shows these displacements superimposed on the first image frame.

In order to further illustrate the accuracy of our computations, and to confirm our statement regarding the normal and the tangential com-

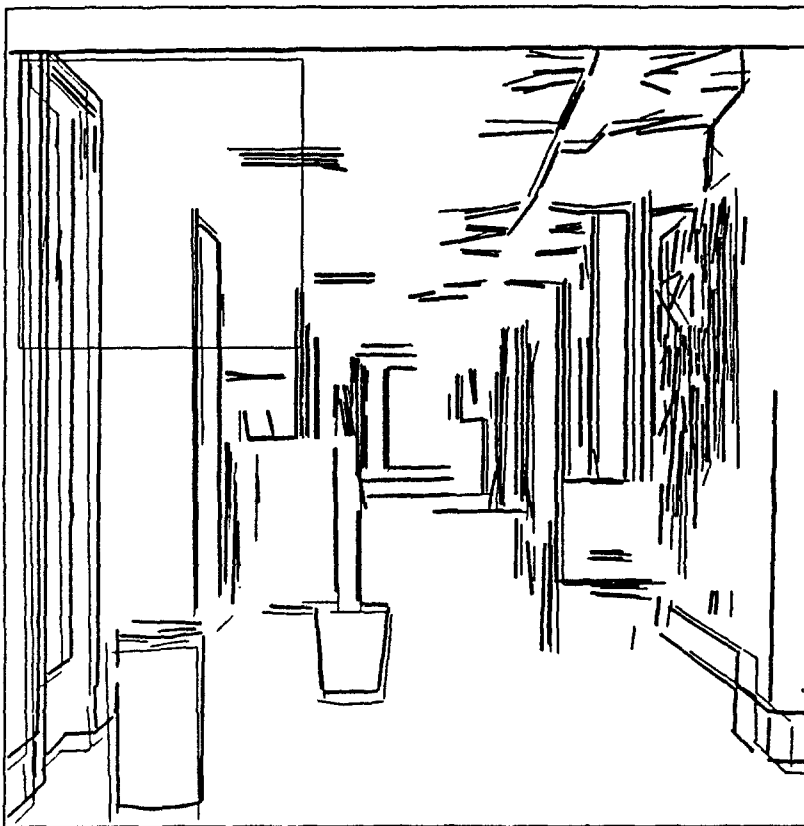


Fig. 15. The hallway-scene experiment—lines. The lines are extracted by Boldt's algorithm from the two input frames. The thick lines are from the first frame; the thin lines are from the second input frame. The area within the rectangular box in the upper left corner of the image will be more closely examined in the next two figures.

ponents, we superimposed our displacement vectors on the set of lines obtained from the two input images by a line-extraction and grouping algorithm developed by Boldt [10,44]. Figure 15 displays the lines extracted from the two images; the lines extracted from the first frame are shown as thick dark lines, while the thinner lines are those obtained from the second frame. Only lines whose associated contrast is greater than 15 grey-levels and which are longer than 7 pixels have been shown. In figures 16 and 17, we have superimposed our displacement vectors on the sets of lines obtained from the two frames in a  $90 \times 90$  pixel area, which is marked in figure 15. Figure 16 displays the *unsmoothed* displacement vectors for a sample of pixels which lie on the lines belong-

ing to the first frame, while figure 17 shows the *smoothed* displacement vectors for the same sample of pixels.

It is obvious from figure 17 that the lines are correctly matched by our displacement vectors. From figure 16, it is clear that the normal components of the unsmoothed vectors are also correct, whereas their tangential components are often incorrect. Finally, the remarkable consistency of the results obtained by Boldt's line-extraction algorithm and our matching algorithm suggests that it may be possible to combine them to extract stable line tokens from image sequences. This idea is currently being pursued at the UMass Computer Vision Laboratory [46].

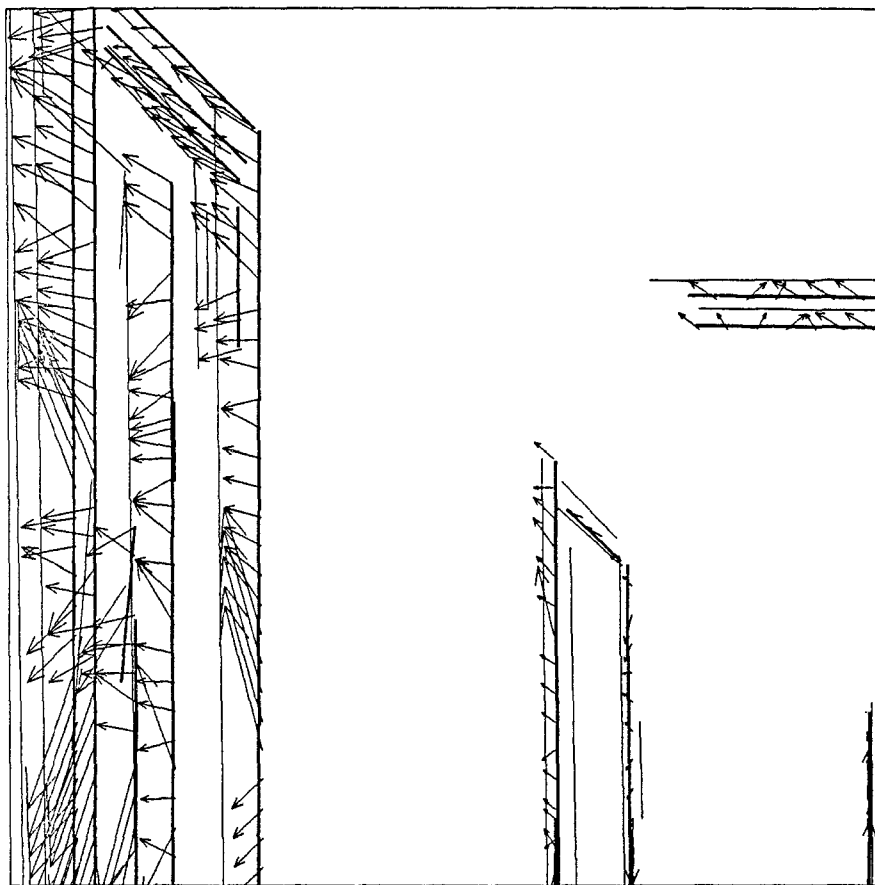


Fig. 16. The hallway-scene experiment—lines with unsmoothed displacements. The unsmoothed displacements are superimposed on the lines extracted by Boldt's algorithm.

## 5 Relationship to the Gradient-Based Techniques

In this section, we describe the general principles underlying the gradient-based techniques for computing image velocity fields, describe two specific gradient-based algorithms, and show that both these techniques are consistent with our framework. Further, we will also show that there is a clear mathematical relationship between the two gradient-based techniques and our matching algorithm.

### 5.1 The Gradient-Based Techniques—An Overview

Almost all the techniques for measuring instantaneous image velocities use the gradient-based

approach. This approach is based on the assumption that the intensity of light reflected by a point on an environmental surface and recorded in the image remains constant during a short time interval, although the location of the image of that point may change due to motion. This assumption leads to the following equation, which is called the *intensity constraint*:

$$|\nabla I|u^\perp = -I_t \quad (6)$$

where  $|\nabla I|$  is the magnitude of the intensity-gradient vector,  $\nabla I = (I_x, I_y)$ ,  $I_t$  is the temporal derivative of the intensity function, and  $u^\perp$  is the component of the image velocity  $\mathbf{u}$  parallel to  $\nabla I$ . The other component  $u^T$ , along the direction perpendicular to  $\nabla I$ , is unspecified by the constraint.

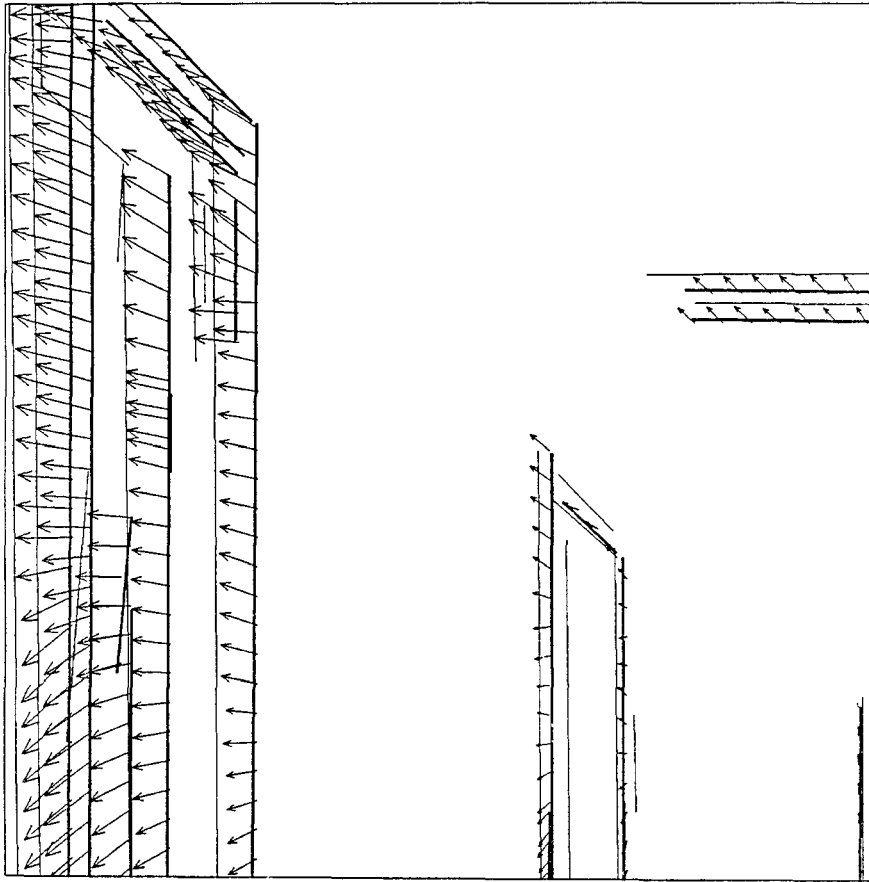


Fig. 17. The hallway-scene experiment—lines with smoothed displacements. The smoothed displacements are superimposed on the lines extracted by Boldt's algorithm.

Since the orientation of the intensity-gradient vector is normal to the direction of the "edge" at a point,  $u^\perp$  and  $u^T$  are respectively called the *normal-flow* and the *tangential-flow* components of the edge. The lack of information regarding the tangential-flow component is known as the *aperture problem* [39].

Since the intensity constraint specifies only one component of the image velocity at a point, an additional constraint is necessary to completely determine the velocity vector; this is usually given in the form of a smoothness constraint on the velocity field [26,27,34]. For this paper, Horn and Schunk's formulation [27] and Nagel's formulation [35] are of particular interest, because they are, respectively, used in the multiresolution gradient-based algorithms of Glazer [21] and En-

kelmann [17]. These two formulations of the smoothness constraints are discussed in detail within the descriptions of the hierarchical techniques given below. It should be noted that both techniques apply the intensity constraint for the computation of displacement. Such an approximation of velocities by displacements is reasonable because of the hierarchical processing schemes used, in which all displacement measurements are small compared to the scale of image intensity variations.

**5.1.1 Enkelmann's Approach.** Enkelmann [17] uses the *low-pass pyramid* transform described by Crowley and Stern [16] to create a set of Gaussian low-pass filters. After the construction of a low-pass pyramid from each image, the processing

begins at a particular coarse level. The description of his technique does not specify how this level is chosen. At the coarsest level, the initial displacement field consists of vectors of zero length. At all other levels the initial displacement field is determined by projecting the field computed at the adjacent coarser level. The projection process involves a bilinear interpolation of the displacement vectors in a small neighborhood of the field at the coarse level.

Within each level, the process of refining the initial displacements is based on Nagel's gradient-based approach [35]. In this approach, an area around each pixel in the image is shifted according to the initial displacement vector at that pixel. The refinement to the initial displacement field is computed by minimizing the functional  $E = E_{\text{int}} + \alpha^2 E_{\text{sm}}$  where  $E_{\text{int}}$  is a formulation of the intensity constraint mentioned above,  $E_{\text{sm}}$  represents the smoothness assumption, and measures the spatial variation of the displacement field, and  $\alpha$  indicates the relative importance attached to the two error terms. Mathematically,

$$E_{\text{int}} = \iint dx dy (I(x,y) - J(x + u, y + v))^2 \quad (7)$$

and

$$E_{\text{sm}} = \iint dx dy \text{trace} [(\nabla \mathbf{u}^T)^T \mathbf{W} (\nabla \mathbf{u}^T)] \quad (8)$$

where  $I$  is the intensity function of the first image;  $J$  is the intensity function of the second image shifted according to the displacements computed from the previous coarse level; and  $\mathbf{W}$  is a weight matrix which depends on the spatial derivatives of the image intensity function  $\mathbf{I}$ . In particular  $\mathbf{W}$  is chosen to allow the propagation of the smoothness constraint along directions with small or no variation of image intensities, while attempting to prevent its propagation along directions with large variations in the intensities. This corresponds roughly to the intuition that large intensity variations may be indicative of region or surface boundaries.

By using the Euler-Lagrange equations, and ignoring the second-order terms of  $(u, v)$ , as well as the third- and higher-order spatial derivatives of the intensity function, the functional minimization problem is transformed to that of solving the

following differential equations:

$$\mathbf{A}\mathbf{u} + \mathbf{b} - \alpha^2 \begin{bmatrix} \text{trace} \{ \mathbf{W} \nabla \nabla u \} \\ \text{trace} \{ \mathbf{W} \nabla \nabla v \} \end{bmatrix} = 0 \quad (9)$$

where

$$\mathbf{A} = (\nabla I)(\nabla I)^T + \bar{x}^2 (\nabla \nabla I)(\nabla \nabla I)^T \quad (10)$$

and

$$\mathbf{b} = \Delta I (\nabla I) + \bar{x}^2 (\nabla \nabla I) \nabla (\Delta I) \quad (11)$$

where  $\Delta I$  is the temporal change in intensity at the image location  $(x, y)$ , the  $\nabla \nabla$  operator represents the matrix of second derivatives, i.e.,

$$\nabla \nabla I = \begin{pmatrix} I_{xx} & I_{xy} \\ I_{xy} & I_{yy} \end{pmatrix}$$

and  $\bar{x}^2$  denotes the size of a small image window which represents the location  $(x, y)$ . Note that in the limit, when the time interval between the two frames tends to zero, the displacements in the above differential equation can be replaced by the corresponding image velocities, provided  $\Delta I$  is replaced by  $I_t$ , the temporal intensity derivative.

By using the finite-difference approach, the differential equations are further transformed into a large sparse system of linear equations. These linear equations are then solved using a multiresolution relaxation approach. The details of the relaxation process are not relevant for the purposes of this paper, although they may be important for an efficient implementation.

*5.1.2 Glazer's Approach.* Glazer also uses a Gaussian low-pass pyramid representation of the input images and employs a hierarchical version of the Horn and Schunck approach. However, the exact algorithm for the construction of the pyramid is different; Glazer uses Burt's Gaussian-pyramid transformation described in [11]. After the construction of the low-pass pyramids, the processing begins at a coarse level at which the magnitudes of the displacements are expected to be less than a pixel. A coarse-to-fine control strategy is used. The projection of the displacements between adjacent levels is structured via the quad-tree connectivity, wherein each pixel at a coarse level is regarded as the "parent" of four pixels at the adjacent finer level. Each "child" uses the dis-

placement of the parent pixel as its initial displacement.

As in Enkelmann's approach, a window around each pixel in the first image is shifted according to the initial displacement at that pixel. The refinement process also consists of minimizing the sum of two functionals  $E_{\text{int}}$  and  $E_{\text{sm}}$ , which represent the intensity constraint and the smoothness assumption respectively. Glazer defines the two errors as

$$E_{\text{int}} = \iint dx dy |\nabla I|^2 (u^\perp - v^\perp)^2 \quad (12)$$

and

$$E_{\text{sm}} = \iint dx dy (\nabla \mathbf{u}^T)^T (\nabla \mathbf{u}^T) \quad (13)$$

As before,  $u^\perp$  is the component of the displacement vector  $\mathbf{u}$  parallel to the intensity-gradient vector  $\nabla I$ , and  $v^\perp = -\Delta I / |\nabla I|$ . Once again, replacing  $\Delta I$  by  $I_t$  leads to a similar equation involving the image velocity  $\mathbf{u}$ .

Glazer also uses the Euler-Lagrange equations to transform this problem into a set of differential equations, and obtains a system of linear equations by using the finite-difference approach. The set of differential equations he obtains are,

$$\nabla I [(\nabla I)^T \mathbf{u} + I_t] - \alpha^2 \begin{bmatrix} \text{trace} \{ \nabla \nabla u \} \\ \text{trace} \{ \nabla \nabla v \} \end{bmatrix} = 0 \quad (14)$$

where the operator  $\nabla \nabla$  is as defined above.

Finally, Glazer uses a multiresolution relaxation process to solve his system of equations, although his approach is more complex than Enkelmann's method and is based on recent theoretical work concerning general multilevel relaxation techniques. The hierarchical gradient-based approach and multilevel relaxation are both described in detail in [21].

## 5.2 Relating the Gradient-Based Techniques to Our Framework

The five components described in section 2 are common to the various techniques that are unified within our framework. The techniques differ in the particular algorithmic choices made for the various components.

It should be evident from the description given in section 3 that our matching algorithm is completely consistent with the framework. In this section, we will show that both the hierarchical gradient-based techniques described above are also consistent with the framework; in the process of showing their consistency with the framework, we will also identify the algorithmic choices made in these two techniques for the various components. Finally, we will establish a mathematical relationship between the gradient-based techniques and the matching algorithm.

From the descriptions given above, it should be obvious that both Enkelmann and Glazer use spatial-frequency channels, and a coarse-to-fine control strategy. In particular, both use Gaussian low-pass filters—although the use of band-pass filters may be more appropriate, because they provide a greater separation of the spatial-frequencies. The control strategy is similar to ours, except for some differences in the projection scheme. The use of the smoothness constraint is also explicit and the various formulations of the smoothness error functional are similar, the primary difference being the use of the weight matrix  $\mathbf{W}$  by Enkelmann.

Although at first sight, the use of the term *match criterion* seems inappropriate for the gradient-based techniques, a careful examination of our definition of the term *match criterion* indicates that the use of the term is valid. According to our definition in section 2, a match criterion is the basis of computing local estimates of the displacements (and more generally, measurements of image motion). In both the gradient-based techniques under consideration, the local estimates are based on the *intensity constancy* assumption. However, in neither technique are the match criterion and the confidence measure explicitly identified. Instead, these are implicitly present in the formulation of the minimization problems. Our purpose here is to explicitly identify these two components in each of the two gradient-based techniques, and demonstrate that an elegant mathematical relationship exists between our matching technique and the two gradient-based techniques.

**5.2.2 Enkelmann's Technique.** As noted earlier, Enkelmann minimizes the sum of the two



functionals  $E_{\text{int}}$  and  $E_{\text{sm}}$ , as defined in equations 7 and 8. Recall also that by using Euler-Lagrange equations, Enkelmann derives the differential equation shown in equation 9. It is easy to show (see [6] for details) that solving this differential equation is also equivalent to minimizing  $E' = E_{\text{sm}} + E'_{\text{int}}$ , where  $E_{\text{sm}}$  is as defined by Enkelmann, and

$$E'_{\text{int}} = \iint dx dy (\mathbf{u} - \mathbf{d})^T \mathbf{A} (\mathbf{u} - \mathbf{d}) \quad (15)$$

In this definition,  $\mathbf{d}$  is any vector such that  $\mathbf{A}\mathbf{d} = -\mathbf{b}$ , and  $\mathbf{A}$  and  $\mathbf{b}$  are as defined in equations (10) and (11). By doing some further algebraic manipulation, it is easy to show that

$$E'_{\text{int}} = \iint dx dy [\lambda_1((\mathbf{u} - \mathbf{d}) \cdot \hat{\mathbf{e}}_1)^2 + \lambda_2((\mathbf{u} - \mathbf{d}) \cdot \hat{\mathbf{e}}_2)^2] \quad (16)$$

where  $\lambda_1$  and  $\lambda_2$  are the two eigenvalues of  $\mathbf{A}$ , and  $\hat{\mathbf{e}}_1$  and  $\hat{\mathbf{e}}_2$  are the associated unit eigenvectors.

The transformation of Enkelmann's  $E_{\text{int}}$  to the form shown in equation 16 allows us to explicitly identify the match constraint and the confidence measures used in his technique. Specifically, the following interpretation is possible: the local estimates of displacement are the solutions to the equation  $\mathbf{A}\mathbf{u} = -\mathbf{b}$ ; corresponding to the components of the solution vector along the directions of the eigenvectors  $\hat{\mathbf{e}}_1$  and  $\hat{\mathbf{e}}_2$  of  $\mathbf{A}$ , we can associate confidence measures  $\lambda_1$  and  $\lambda_2$  respectively. Note that while we can guarantee that there is at least one solution to this equation (see [6]), there is no guarantee that such a solution will be unique. In particular, it is easy to see that if both the eigenvalues of  $\mathbf{A}$  are nonzero, there will be a unique solution vector ( $\mathbf{d}$ ); whereas if any of the eigenvalues are zero, the component of the solution vector along the direction of the corresponding vector can be arbitrarily chosen. In fact, the underlying image pixel can be regarded as a corner, edge, or a homogeneous area according to whether the matrix  $A$  has 2, 1, or 0 nonzero eigenvalues.

**5.2.3 Glazer's Technique.** The definition of  $E_{\text{int}}$  used by Glazer is the following:

$$E_{\text{int}} = \iint dx dy |\nabla I|^2 (u^\perp - v^\perp)^2 \quad (17)$$

where  $v^\perp = -\Delta I / |\nabla I|$ . If the parameter  $\bar{x}^2$ , which represents the window size in the definitions of  $\mathbf{A}$  and  $\mathbf{b}$  is set to zero, the equation  $\mathbf{A}\mathbf{u} = -\mathbf{b}$  reduces to the equation

$$(\nabla I)^T \mathbf{u} = -I,$$

which is equivalent to the normal-flow equation (6). Moreover, it can be shown that in this case,

$$\lambda_1 = 0, \quad \lambda_2 = |\nabla I|^2, \quad \text{and } \hat{\mathbf{e}}_1 = \hat{\mathbf{e}}_{vI} \quad (18)$$

Thus, we see that Glazer's choice for the local estimates of motion and the confidence measures are similar to Enkelmann's, with the important difference that the size of the window representing a point tends to zero, i.e., the window shrinks to a point.

#### 5.2.4 The Mathematical Relationship Between the Matching and the Gradient-Based Approaches.

Thus far, we have shown that the two gradient-based techniques contain all the components of our framework, and are therefore completely consistent with it. In addition, we have also shown that Glazer's first-order gradient-based estimates of motion and the associated confidences are the values obtained by using Enkelmann's approach in the limiting case (when the window size tends to zero). Here, we also note that there is a close mathematical relationship between our matching approach and the gradient-based approaches. The following theorem summarizes this relationship:

**THEOREM.** *In the limit, when the interframe time interval tends to zero, the formulation of the approximation error for image displacements used in the discrete-matching approach converges to the second-order formulation of  $E_{\text{int}}$  for image velocities used in the gradient-based approach, provided the third- and higher-order spatial intensity derivatives are ignored. Further, when the window size represented by  $\bar{x}^2$  tends to zero,  $E_{\text{app}}$  converges exactly to the first-order gradient-based formulation of  $E_{\text{int}}$ .*

The proof of this theorem is too long for this paper, and can be found in [6]. The general approach is based on a derivation of Nagel [33] that in the limiting case (when the interframe time interval tends to zero), the minimization of the SSD

measure is equivalent to solving the equation  $\mathbf{A}\mathbf{u} = -\mathbf{b}$ .

### 5.3 Discussion

Thus far, we have attempted to establish the consistency of the gradient-based techniques with our framework, and describe the mathematical relationship between the gradient-based techniques and our matching technique. We have shown that our framework provides a unifying perspective for the correlation-matching techniques and gradient-based techniques. In particular, the use of multiresolution, multiple-frequency computations, the implicit or the explicit use of a confidence measure, and a smoothness constraint which uses that confidence measure seem essential for the success of all of these techniques.

We have also shown that in the gradient-based techniques, the confidence measure can be isolated from the smoothness assumption. This allows us to retain the confidence measure (which we believe to be essential), but reexamine the formulation of the smoothness assumption, and even consider whether such an assumption is always useful. For example, alternate forms of the smoothness constraint may be easily combined with the local measurements and the associated confidence measures: these include the flow-analyticity constraint of Waxman [43], the stochastic relaxation approaches of [19,31], and other such methods. Alternatively, we can even postpone the construction of a dense displacement field, and use the local measurements and their confidences in a segmentation and grouping technique such as that of Adiv [2].

## 6 Processing Discontinuities in Image Motion

In this section, we consider one of the major unsolved problems in the analysis of visual motion and its relation to our computational framework. This situation involves processing discontinuities in image motion, which are present at the boundaries of surfaces, or at the boundaries of objects. Around the locations of such discontinuities, the

smoothing involved in the spatial-frequency decomposition process creates intensity structures that have no physical correlates. Therefore, the information contained in the lower-frequency channels in the two images will be inconsistent. The local translational assumption and the spectral continuity principles are also violated. Obviously, it would be inappropriate to apply the smoothness constraint across such boundaries.

In order to process discontinuities in image motion, we must first detect such discontinuities. It should be clear from the brief discussion above that the detection of discontinuities cannot be postponed until after the computation of a dense flow field; rather, it should happen simultaneously with that computation. This means that our framework (as well as the techniques consistent with it) should be modified to incorporate the notion of discontinuities in image motion. Here we outline some possible ways to approach this task.

In the current version of our matching algorithm, the confidence measures are normalized according to the magnitude of the minimum SSD value computed during the search process. The minimum SSD value is likely to be large if (i) the search area does not contain the true match (either due to occlusion or due to incorrect coarse-level estimate); (ii) the magnitudes of rotation and translation in depth are large; and (iii) the SNR (signal-to-noise) ratio is low. All these are cases where even the best match (and even if the SSD surface has a sharp minimum) is unreliable. In addition to the magnitude of the minimum SSD value, a significant difference in the shapes of the auto- and cross-SSD surfaces may also indicate an unreliable match.

A local measure of the likelihood of a false match is itself not sufficient to determine the presence of discontinuities. Typically the discontinuities will form a contour on the image plane. The spatial derivative of the image flow field across such a bounding contour can be expected to be large. If these three types of information are combined, the robust detection of discontinuities may be possible.

One way to combine various sources of information to detect discontinuities in image motion is to first obtain a local "no match" measure, and

explicitly include discontinuities in the smoothness process. This is somewhat similar to the approach suggested by Geman and Geman [19] for edge detection, and more recently by Marroquin et al. [31] for surface reconstruction from sparse depth data. The advantage of this approach is that by using two coupled models, one for the flow field, and the other for the discontinuity boundaries, the discontinuity detection process is dynamic and explicitly encoded.

## 7 Summary

We have described a hierarchical computational framework for the determination of dense displacement fields from a pair of images. We have also developed a matching algorithm consistent with our framework and demonstrated its performance on real images.

Our framework is sufficiently general in order to unify the gradient-based and the matching techniques. In particular, we have shown that in addition to our own technique, two successful gradient-based techniques are consistent with our framework. We have also established a clear mathematical relationship between the gradient-based techniques and our matching technique.

At present, the detection and processing of discontinuities in image motion is difficult. Also, our current approach (and for that matter almost all the current approaches for the measurement of motion) is not capable of processing scenes containing transparent or fence-like surfaces. Finally, we have not addressed the issues involved in processing multiple frames. While these problems form the obvious basis for further research in the measurement of visual motion, we wish to note that our algorithm is readily applicable to a large class of commonly encountered images and performs robustly (see [6]) with almost no adjustment of parameters.

## Acknowledgements

The author wishes to thank Profs. Edward Riseman and Allen Hanson for their continued advice and support through the course of this work.

Thanks are also due to George Reynolds, Prof. Riseman, Prof. Hanson, and Michael Boldt for their comments on earlier drafts, to Richard Weiss and Mark Snyder for their help with some of the mathematical aspects of this research, and to Poornima Balasubramanyam for a careful reading of the final draft. Finally, thanks are due to the members of the UMass VISIONS group for creating a unique and valuable research environment.

The research described in this paper was conducted at the Computer Vision Laboratory at University of Massachusetts, Amherst and was supported by DARPA under grant N00014-82-K-0464.

## References

1. E.H. Adelson and J.R. Bergen, "Spatiotemporal energy models for the perception of motion," *J. Opt. Soc. Am. A*, 2(2):284-299, 1985.
2. G. Adiv, "Determining 3-D motion and structure from optical flows generated by several moving objects," *IEEE Trans. PAMI* 7(4):384-401, 1985.
3. G. Adiv, "Inherent ambiguities in recovering 3-D motion and structure from a noisy flow field," *Proc. Conf. Comput. Vision and Pattern Recognition*, pp. 70-77, 1985.
4. J.K. Aggarwal, L.S. Davis, and W.N. Martin, "Correspondence processes in dynamic scene analysis," *Proc. IEEE* 69(5):562-572, 1981.
5. P. Anandan, "Computing dense displacement fields with confidence measures in scenes containing occlusion," *SPIE Int. Conf. Robots and Comput. Vision*, 521:184-194, 1984; also as COINS Tech. Rept. 84-32, Univ. of Massachusetts, December 1984.
6. P. Anandan, "Measuring visual motion from image sequences," PhD dissertation, COINS TR 87-21, Univ. of Massachusetts, Amherst, MA, 1987.
7. P. Anandan and R. Weiss, "Introducing a smoothness constraint in a matching approach for the computation of displacement fields," *Proc. DARPA IU Workshop* pp. 186-196, 1985.
8. S.T. Barnard and W.B. Thompson, "Disparity analysis of images," *IEEE Trans. PAMI* 2(4):333-340, 1980.
9. P. Beaudet, "Rotationally invariant image operators," *Proc. Int. Conf. Pattern Recognition*, pp. 579-583, 1978.
10. M. Boldt and R. Weiss, "Token-based extraction of straight lines," COINS TR 87-104, Univ. of Massachusetts, Amherst, MA, 1987.
11. P.J. Burt, "Fast filter transforms for image processing," *Comput. Graphics Image Processing* 16:20-51, 1981.
12. P.J. Burt, T.H. Hong, and A. Rosenfeld, "Image segmentation and region property computation by cooperative hierarchical computation," *IEEE Trans. Syst., Man, Cybern.* 11:802-809, 1981.

13. P.J. Burt, C. Yen, and X. Xu, "Local correlation measures for motion analysis: A comparative study," *Proc. IEEE Conf. Pattern Recognition Image Processing*, pp. 269-274, 1982.
14. P.J. Burt, C. Yen, and X. Xu, "Multiresolution flow-through motion analysis," *Proc. IEEE Conf. Comput. Vision Pattern Recognition*, pp. 246-252, 1983.
15. M.P. do Carmo, *Differential Geometry of Curves and Surfaces*. Prentice-Hall: Englewood Cliffs, NJ, 1976.
16. J.L. Crowley and R.M. Stern, "Fast computations of the difference of low-pass transform," *IEEE Trans. PAMI* 6:212-222, 1984.
17. W. Enkelmann, "Investigations of multigrid algorithms for the estimation of optical flow fields in image sequences," *Proc. Workshop Motion: Representation and Control*, Kiawah Island, SC, 1986, pp. 81-87.
18. J. Fang and T.S. Huang, "Some experiments on estimating the 3-D motion parameters of a rigid body from two consecutive image frames," *IEEE Trans. PAMI* 6(5):545-554, 1984.
19. S. Geman and D. Geman, "Stochastic relaxation, Gibbs distributions, and the Bayesian restoration of images," *IEEE Trans. PAMI* 6(6):721-741, 1984.
20. D. Gennery, "Modeling the environment of an exploring vehicle by means of stereo vision," PhD dissertation, Standard Artificial Intelligence Laboratory, AIM-339, 1980.
21. F. Glazer, "Hierarchical motion detection." PhD dissertation, COINS TR 87-02, Univ. of Massachusetts, Amherst, MA, 1987.
22. F. Glazer, G. Reynolds, and P. Anandan, "Scene matching by hierarchical correlation," *Proc. IEEE Conf. Comput. Vision and Pattern Recognition*, Annapolis, MD, pp. 432-441, 1983.
23. W.E.L. Grimson, "Computational experiments with a feature based stereo algorithm," *IEEE Trans. PAMI* 7(1):17-34, 1985.
24. A.R. Hanson and E.M. Riseman, "Processing cones: A computational structure for image analysis." In *Structured Computer Vision*, S. Tanimato and A. Klinger (eds.), Academic Press: New York, 1980.
25. D. Heeger, "Optical flow from spatiotemporal filters," *Proc. 1st Int. Conf. Comput. Vision*, London, UK, pp. 181-190, 1987.
26. E.C. Hildreth, *The Measurement of Visual Motion*. MIT Press: Cambridge, MA, 1984.
27. B.K.P. Horn and B.G. Schunck, "Determining Optical Flow," *Artificial Intelligence* 17:185-203, 1981.
28. A. Klinger and R.D. Dyer, "Experiments on picture representations using regular decomposition," *Comput. Graphics Image Processing* 5(1):68-105, 1976.
29. B.D. Lucas and T. Kanade, "An iterative image registration technique with an application to stereo vision," *Proc. 7th Int. Joint Conf. Artif. Intell.*, Vancouver, Canada, pp. 674-679, 1981.
30. D. Marr and T. Poggio, "A computational theory of human stereo vision," *Proc. Roy. Soc. London B-204*, pp. 301-308, 1979.
31. J. Marroquin, S. Mitter, and T. Poggio, "Probabilistic solutions for ill-posed problems in computational vision," *Proc. DARPA IU Workshop*, Miami Beach, FL, pp. 293-309, 1986.
32. J.E.W. Mayhew and J.P. Frisby, "Psychophysical and computational studies towards a theory of human stereopsis," *Artificial Intelligence* 17:349-385, 1981.
33. H.H. Nagel, "Displacement vectors derived from second order intensity variations in image sequences," *Comput. Vision Pattern Recognition Image Processing* 21:85-117, 1983.
34. H.H. Nagel, "Image sequences—ten (octal) years—from phenomenology towards a theoretical foundation," *Proc. 8th Int. Conf. Pattern Recognition*, Paris, France, 1986.
35. H.H. Nagel and W. Enkelmann, "An investigation of smoothness constraints for the estimation of displacement vector fields from image sequences," *IEEE Trans. PAMI* 8:565-593, 1986.
36. A. Rosenfeld and A.C. Kak, *Digital Picture Processing*. Academic Press: New York, 1976.
37. S.L. Tanimato and T. Pavlidis, "A hierarchical data structure for picture processing," *Comput. Graphics Image Processing* 4(2):104-119, 1975.
38. D. Terzopoulos, "Multiresolution computation of visible-surface representations," PhD dissertation, Massachusetts Institute of Technology, 1984.
39. S. Ullman, "Analysis of visual motion by biological and computer systems," *IEEE Computer*, pp. 57-69, 1981.
40. J.P.H. van Santen and G. Sperling, "Elaborated Reichardt detectors," *J. Opt. Soc. Amer.* 2(7):300-321, 1985.
41. A.B. Watson and A.J. Ahmuda, "Model of human visual-motion sensing," *J. Opt. Soc. Amer.* 2(7), 1985.
42. A. Waxman, "An image-flow paradigm," *Proc. Workshop Comput. Vision*, Annapolis, MD, pp. 49-57, 1984.
43. A. Waxman and K. Wahn, "Contour evaluation, neighborhood deformation, and global image flow: planar surfaces in motion," *Univ. of Maryland Tech. Rept. CS-TR-1394*, 1984.
44. R. Weiss and M. Boldt, "Geometric grouping applied to straight lines," *Proc. IEEE Conf. Comput. Vision Pattern Recognition*, Miami Beach, FL, pp. 489-493, 1986.
45. L.R. Williams and P. Anandan, "A coarse-to-fine control strategy for stereo and motion on a mesh-connected computer," *Proc. IEEE Conf. Comput. Vision Pattern Recognition*, Miami Beach, FL, pp. 219-226, 1986.
46. L.R. Williams and A. Hanson, "Translating optical flow into token matching," *Proc. DARPA IU Workshop*, Boston, MA, pp. 970-980, 1988.
47. R.Y. Wong and E.L. Hall, "Sequential hierarchical scene matching," *IEEE Trans. Comput.* 27(4):359-366, 1978.